Electronic Supplementary Material (ESI) for CrystEngComm.

Supporting Information

Formation of amorphous calcium carbonate and its transformation into mesostructured calcite

Carlos Rodriguez-Navarro,[a] Krzysztof Kudłacz,[b] Özlem Cizer[c] and Encarnacion Ruiz-Agudo[a]*

[a] University of Granada, Department of Mineralogy and Petrology, Granada, Spain.

[b]Institute of Metallurgy and Materials Science, Polish Academy of Sciences, Reymonta 25, 30-059 Kraków, Poland.

[c]KU Leuven, Department of Civil Engineering, Leuven, Belgium.

*Corresponding author e-mail: carlosrn@ugr.es

Table of contents **Page**

Supplementary Table

Table S1. Solubility product, k_{sp} and dissolution enthalpy, ΔH_{diss} of calcite, aragonite, vaterite, hydrated ACC and anhydrous ACC (at STP).

	k_{sp}	References	ΔH_{diss} (kJ/mol)	References
Calcite	3.98×10^{-9}	1	-28.75	4
Aragonite	4.61×10^{-9}	1	-31.44	5
Vaterite	1.22×10^{-8}	1	-36.30	6
$ACC_{hydrated}$	9.10×10^{-7}	2,3	-52.02*	4
$ACC_{anhydrous}$	9.92×10^{-8}	This study	-43.45	4

* This value corresponds to the average of ΔH_{diss} values reported in Supplementary ref. (4) for the more disordered (more metastable) synthetic ACCs.

Supplementary figures

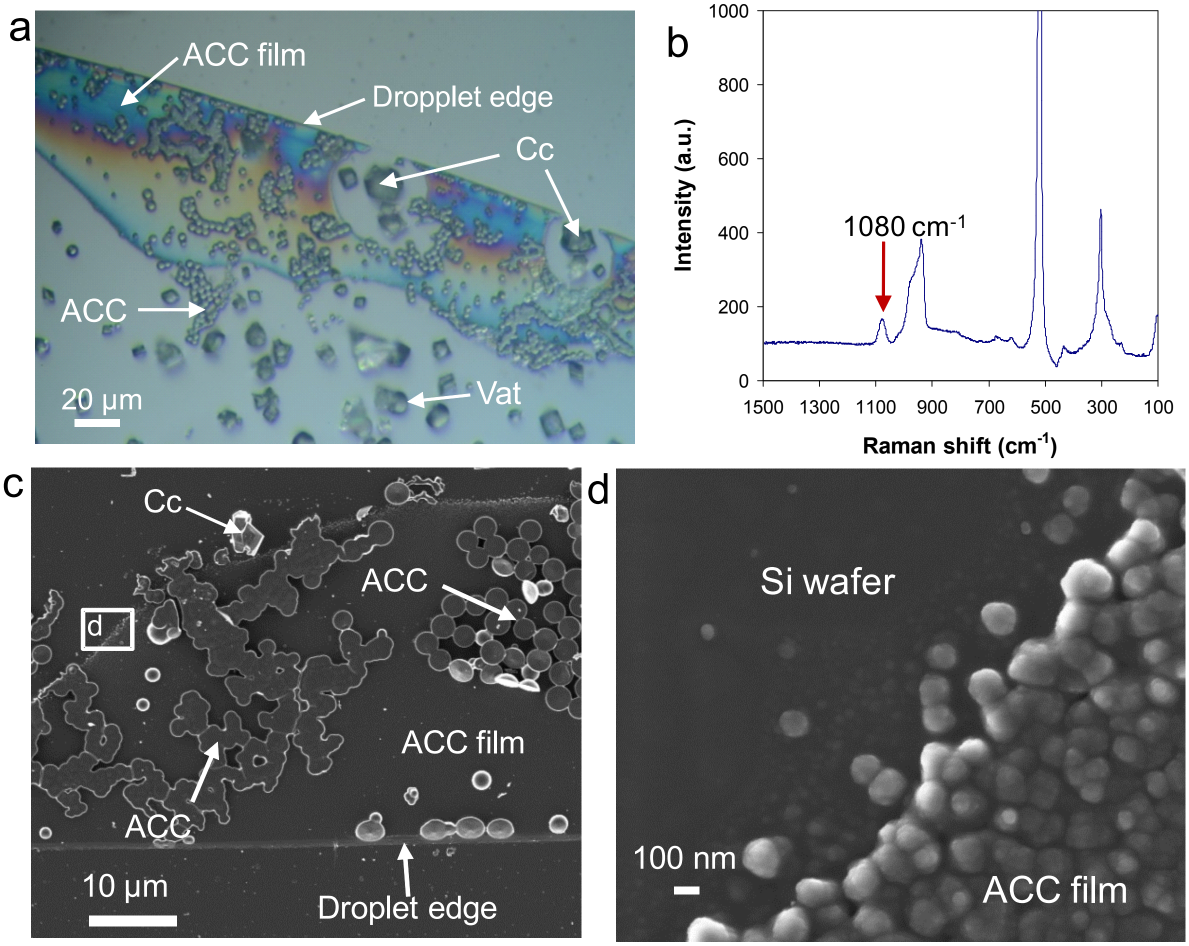

Figure S1. Precipitates formed upon solution droplet carbonation and drying: (a) optical microscopy (reflected plane light) and (c) FESEM images of ACC film, ACC hemispheres (ACC), vaterite (vat) and calcite (Cc) deposited on a Si wafer; (b) Raman spectra of the ACC film showing the characteristic peak at 1084 cm^{-1} (red arrow). Note that all other bands correspond to the Si wafer; (d) detail of the ACC film in squared section of (c).

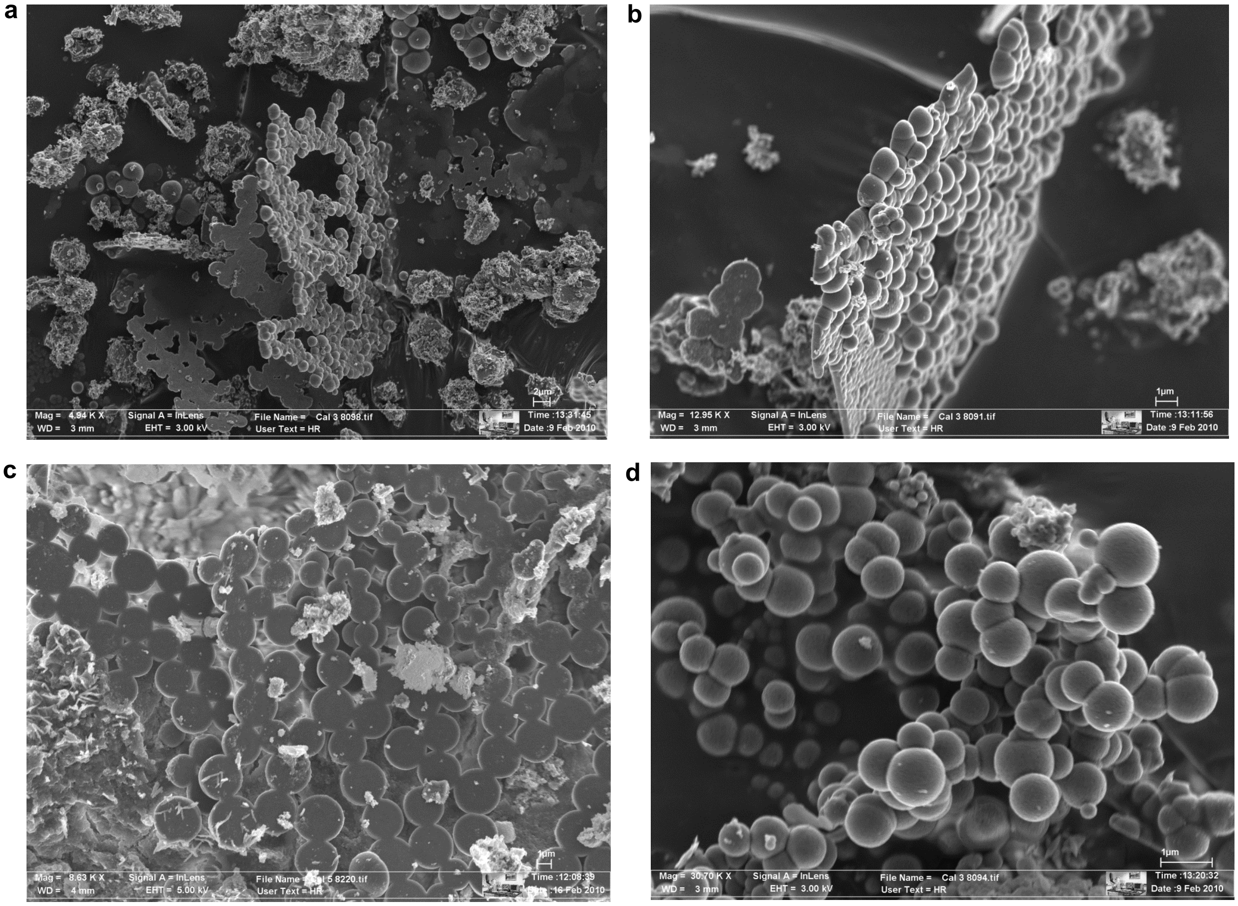

Figure S2. FESEM photomicrographs of precipitates formed after carbonation of $Ca(OH)_2$ solution in droplets (a-c) and batch reactor (d) tests: a) general view of ACC precipitates; b) detail of an aggregate of ACC hemispheres which resemble a “microlens array”; c) same as (b) but observed from the opposite side of the aggregate (i.e., the flat surface of hemispheres facing the air during precipitation); d) aggregate of ACC particles formed in the bulk solution.

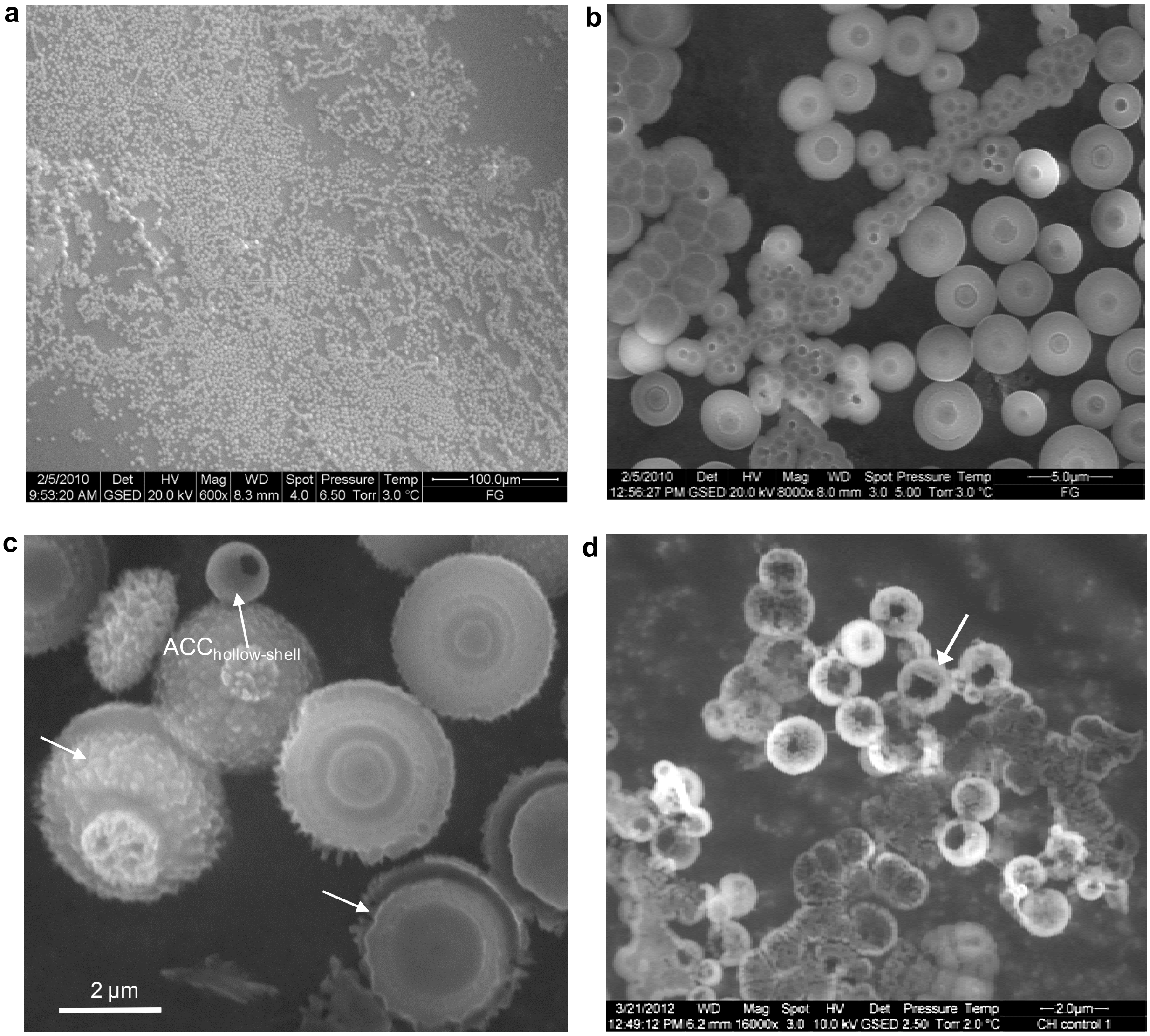

Figure S3. In situ ESEM observation of ACC precipitation and dissolution: a) general overview of precipitates formed at the air/solution interface upon air exposure of the $Ca(OH)_2$ solution for 5 min prior to ESEM imaging; b) dissolution features in ACC hemispheres after 15 min carbonation time; c) detail of non-homogeneous dissolution of ACC hemispheres and hollow-shell ACC sphere; d) dissolution of ACC particles showing that they are hollow-spheres. Some of them show a final doughnut-shaped morphology (arrow) which is also observed under the TEM (see Figure 3).

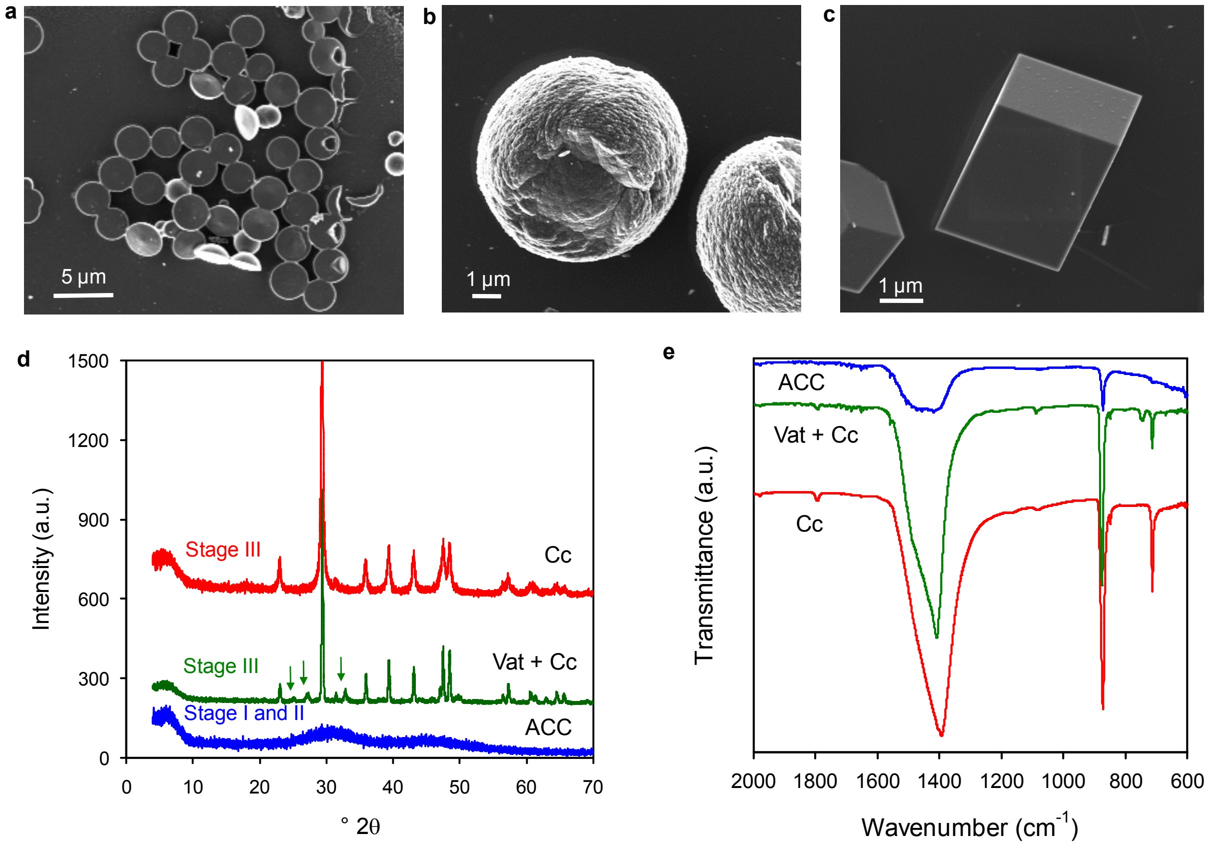

Figure S4. *Ex situ* analysis of precipitates formed in droplets and batch reactors. FESEM images of ACC hemispheres (some of them partially dissolved) (a), vaterite (b) and calcite (c) deposited on Si wafers (droplets experiments); d) XRD patterns and e) FTIR spectra of precipitates collected from batch reactors during Stage I and II (ACC), Stage III (ACC plus calcite –Cc- and vaterite –Vat-, green arrows) and after completion of Stage III (calcite).

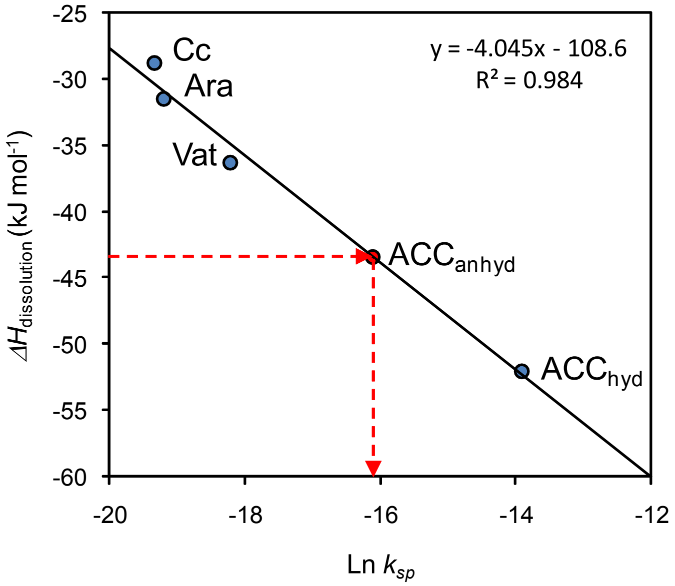

Figure S5. Relationship between ln k_{sp} of the different calcium carbonate phases and their enthalpy of dissolution, ΔH_{diss}. Blue-filled circles represent published values for hydrated ACC (ACC$_{\mathrm{hyd}}$), aragonite (Ara), vaterite (Vat) and calcite (Cc). The red-filled circle shows the calculated k_{sp} value (see dashed arrows) of anhydrous ACC (ACC$_{\mathrm{anhyd}}$) determined using the fitted linear regression (equation in inset) and the ΔH_{diss} value reported by Rahda *et al*.[4]

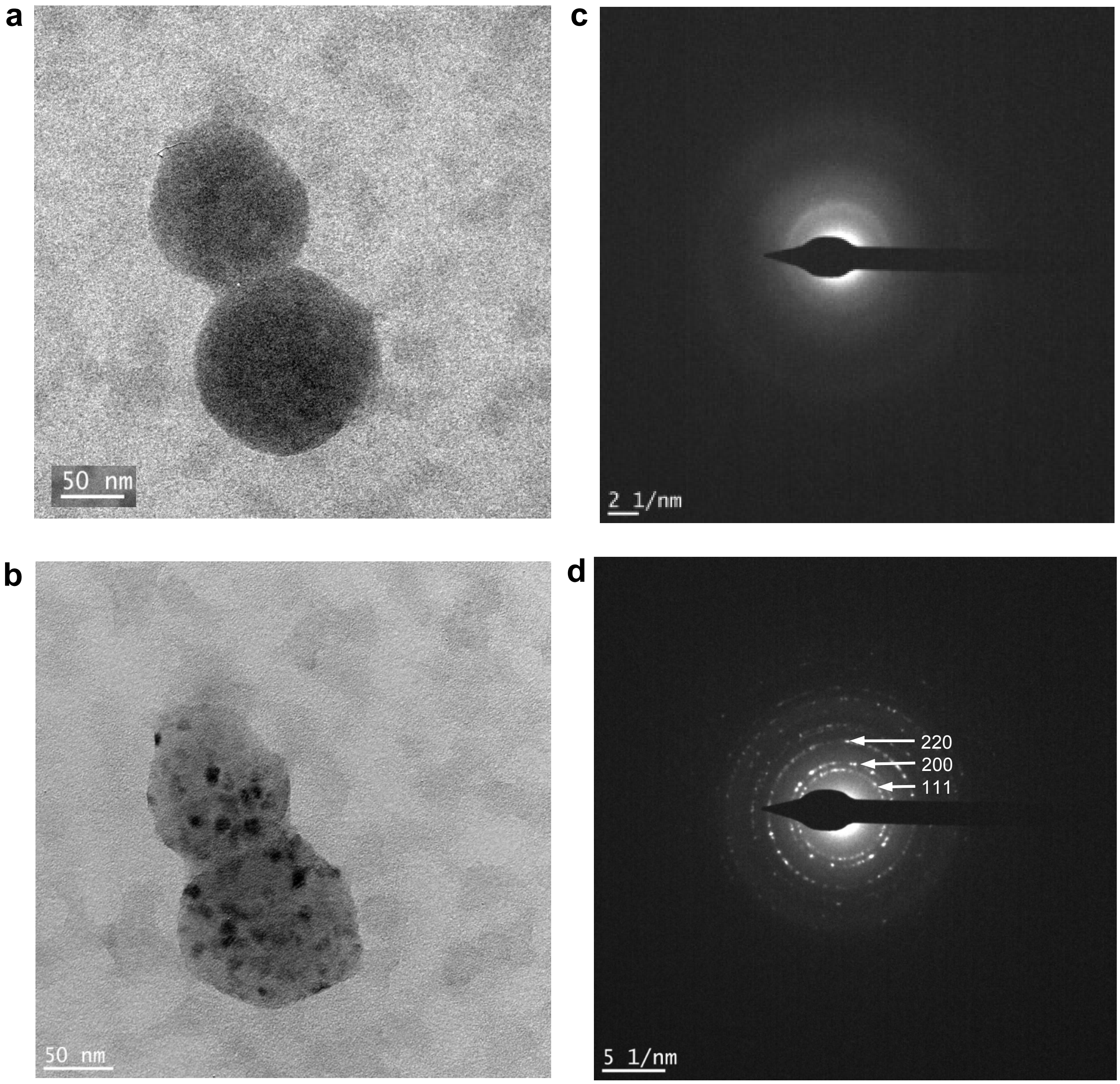

Figure S6. TEM-SAED images of ACC particles formed during Stage I before (a) and after (b) focused electron-beam irradiation for 30 s. The corresponding SAED patterns are shown in c) and f). Following e-beam irradiation the particles shrink due to water release, resulting in the direct formation of CaO (note that CO_2 release upon e-beam irradiation does not result in shrinking, but in mesopore formation).[7] The spotted Debye rings correspond to the main Bragg reflections of lime and show that individual oxide nanocrystals, which show dark orientation contrast in (b), are randomly oriented.

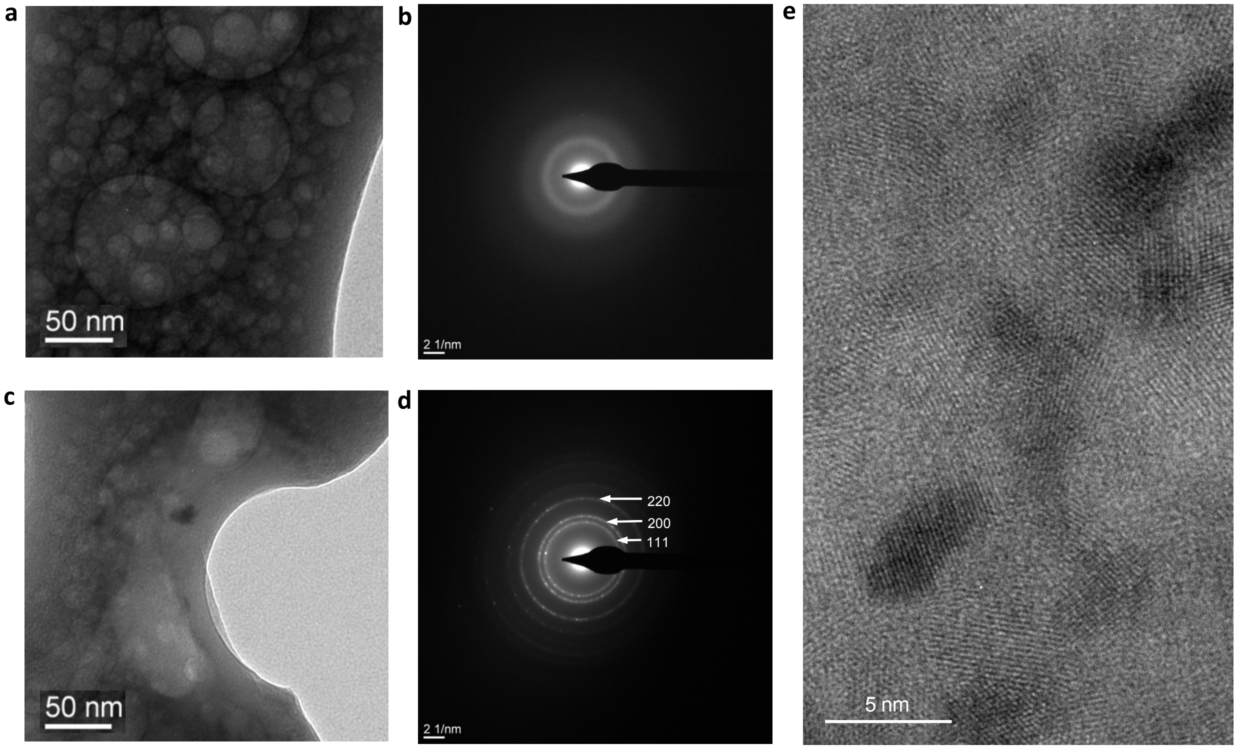

Figure S7. TEM photomicrographs of an ACC particle before (a) and after (c) focused e-beam irradiation. The corresponding SAED patterns are shown in (b) and (d). Note that the initial ACC particle is made up of an aggregate of polydisperse nanoparticles which apparently started to dehydrate under the electron beam, thereby producing water vapor bubbles (responsible for the whiter contrast). Upon focused e-beam irradiation significant shrinking and formation of randomly oriented CaO crystals occurs as shown by the nearly continuous Debye rings (d) and the randomly oriented lattice fringes of CaO in the HRTEM image (e).

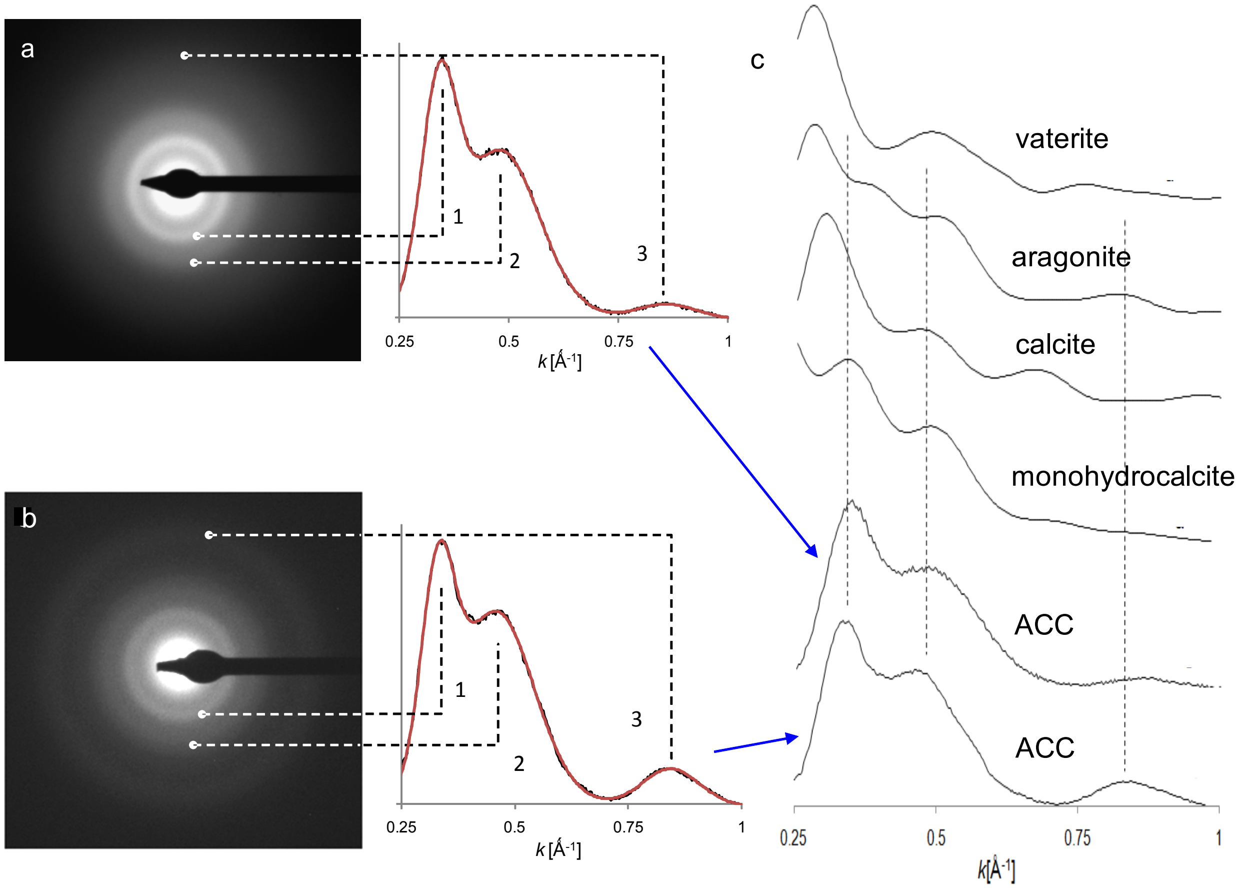

Figure S8. Experimental SAED patterns and corresponding EDPs of two ACC particles formed during Stage II (a, b) and their comparison with simulated EDPs for randomly-oriented clusters with 10 Å cluster size and different internal crystalline structure (c).

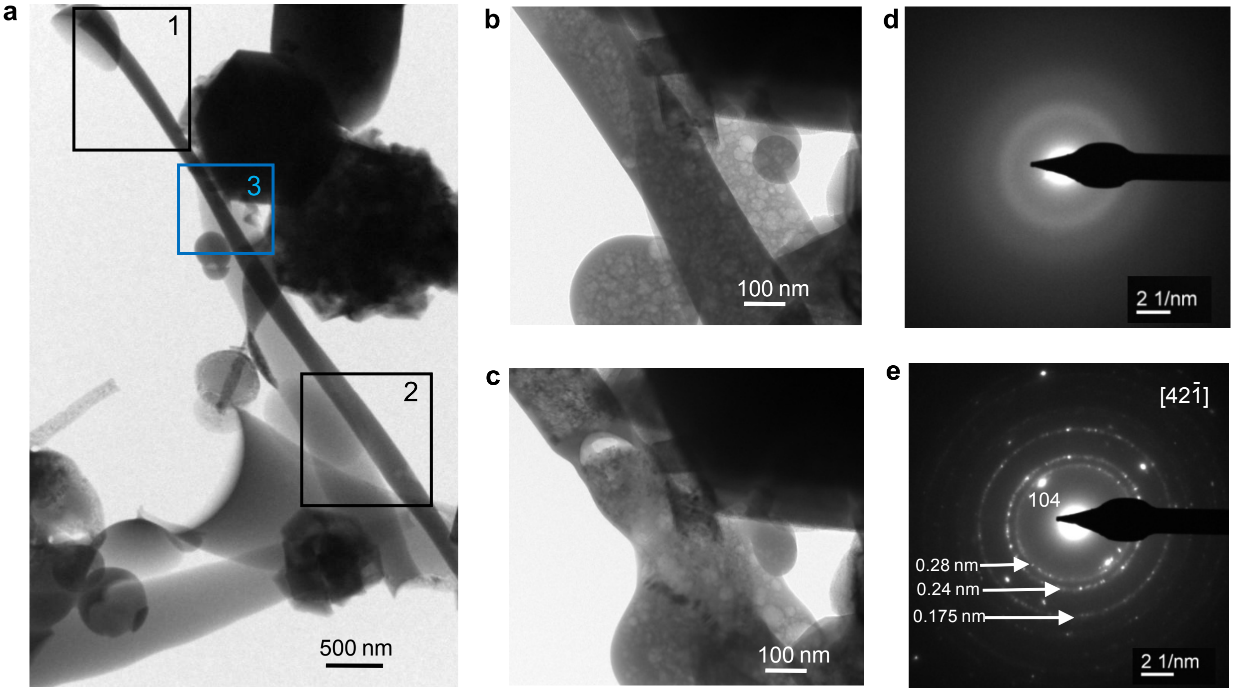

Figure S9. *In situ* transformation of 1D ACC structure formed during Stage II. a) general overview of the elongated ACC fiber showing squared areas 1 and 2 where irradiation was performed as shown in Figure 5; area in square 3 (blue) before (b) and after (c) focused e-beam irradiation; SAED of the area in square 3 of (a) before (d) and after (e) focused e-beam irradiation for 30 s. In addition to calcite oriented along the $[42\bar{1}]$ zone axis (equal orientation as that of calcite formed upon e-beam irradiation in square 1 and 2), spotted Debye rings corresponding to CaO (*d*-spacings of 111, 200 and 222 planes are indicated). The latter phase corresponds to the product of the decomposition of (less stable) hydrated ACC spheres attached to the central 1D ACC structure which undergo significant shrinking and deformation upon e-beam irradiation (c).

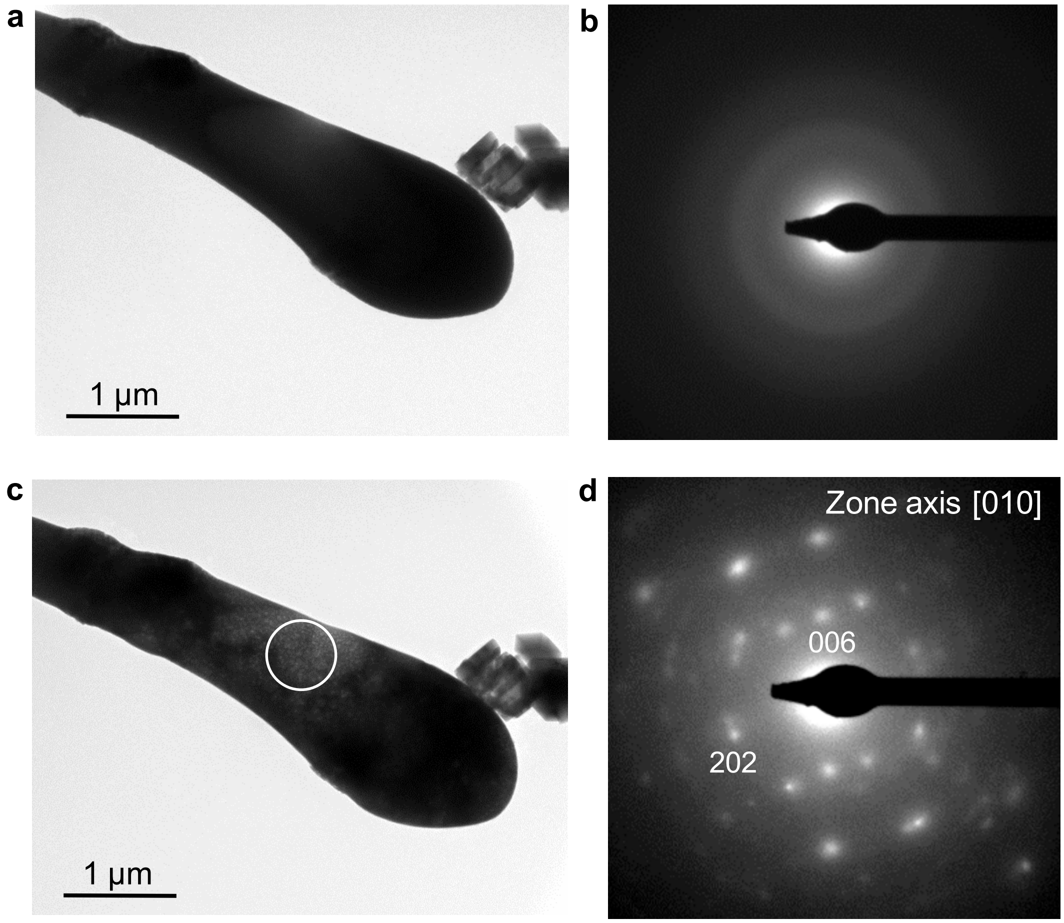

Figure S10. Focused e-beam transformation of ACC particle formed during Stage II. a) ACC before irradiation ; b) SAED of the structure in (a); c) the particle in (a) after 30 s focused e-beam irradiation. Note that there is no volume change, which shows that this ACC is (nearly) anhydrous; d) SAED of irradiated and transformed ACC in (c) showing the [010] zone axis pattern of newly-formed calcite. The angular spreading of diffraction spots (ca. 5º) shows that the resulting calcite is made up of a aggregate of oriented nanocrystals (mesocrystal). The white circle in (c) shows the area where SAED was acquired after transformation. The rhombohedral crystals on the right are calcite directly precipitated from solution.

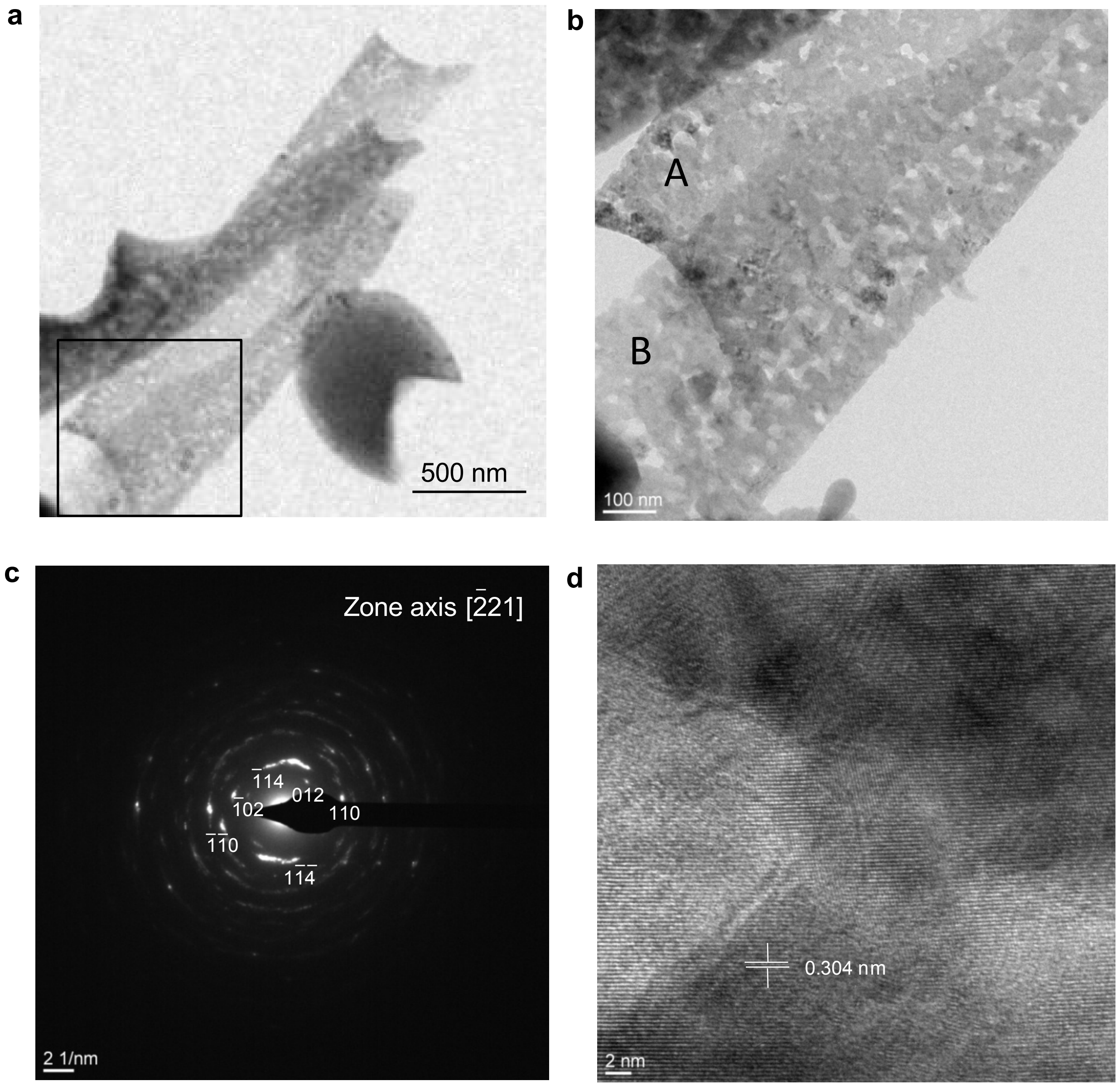

Figure S11. TEM-SAED analysis of ACC structures formed during Stage II and exposed to humid air (85 % RH, 20 °C) for 48 h. a) 2D and 3D ACC structures transformed into porous pseudomorphs of calcite; b) detail of the structure in (a) (squared area); c) its corresponding calcite [$\bar{2}21$] zone axis SAED pattern. Note that the diffraction pattern corresponds to two overlying structures, denoted A and B in (b), which display a ca. 30° rotation around the [$\bar{2}21$] zone axis (explaining why there are two spots for each point of the reciprocal lattice). Each diffraction spot displays an angular spreading is ca. 10°, showing that calcite domains are slightly missoriented; nonetheless, the HRTEM image (d) shows the $104_{calcite}$ lattice fringes that display continuity across domains larger than 30 nm.

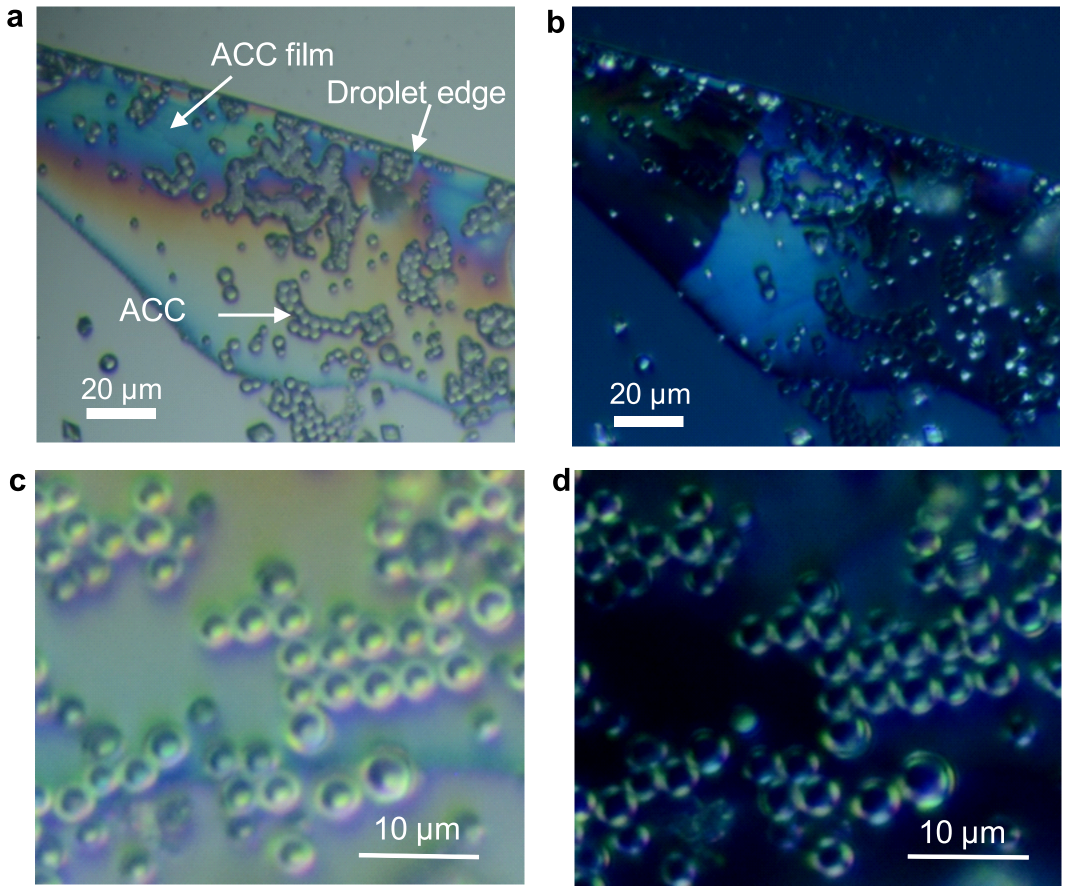

Figure S12. Transformation of hydrated ACC formed during Stage I into calcite upon exposure to humid air (85% RH; 20 °C) for 48 h. Plane light (a) and cross polarized light (b) microscopy image of ACC. The iridescent ACC film formed at the droplet edge during Stage I (Fig. S1) transformed into a mosaic of non-oriented calcite crystals as revealed by the interference color variations shown in (b). Larger ACC hemispheres are also present (c), and upon exposure to humid air pseudomorphically transformed into radial aggregates of calcite (according to micro-Raman spectroscopy) as shown by their Maltese cross (Webster cross) extinction under cross polarized light (d).

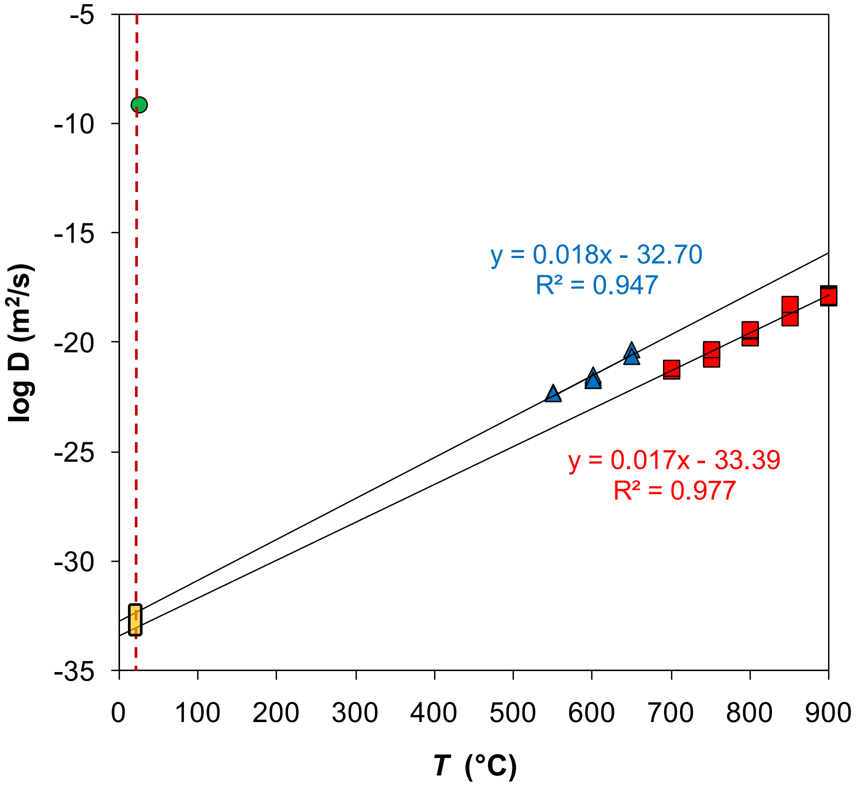

Figure S13. Self-diffusion coefficient, D, of Ca ions in water at room *T* (green circle)[8] and in solid $CaCO_3$ (calcite) at high *T* (blue triangles: data from Supplementary ref. (9); red square, data from Supplementary ref. (10)). Extrapolation of D values for solid-state self-diffusion of Ca ions in calcite to room *T* yields log D values (beige rectangle) of -32.25 to -32.96 m^2s^{-1} (i.e., D values some 23 orders of magnitude smaller than that corresponding to Ca ions self-diffusion in an aqueous solution at room *T*). The red dashed vertical line marks $T = 25$ °C.

Supplementary References

(1) L. N. Plummer and E. Busenberg, *Geochim. Cosmochim. Acta* 1982, **46**, 1011.

(2) T. Ogino, T. Suzuki and K. Sawada, *Geochim. Cosmochim. Acta* 1987, **51**, 2757.

(3) J. R. Clarkson, T. J. Price and C. J. Adams, *J. Chem. Soc. Faraday Trans.* 1992, **88**, 243.

(4) A. V. Radha, T. Z. Forbes, C. E. Killian, P. U. P. A. Gilbert and A. Navrotsky, *Proc. Natl. Acad. Sci. USA* 2010, **107**, 16438.

(5) G. Wolf, J. Lerchner, H. Schmidt, H. Gamsjäger, E. Königsberger, P. Schmidt, *J. Therm. Anal.* 1996, **46**, 353.

(6) G. Wolf, E. Konigsberger, H. G. Schmidt, L. C. Konigsberger and H. Gamsjager, *J. Therm. Anal. Calorim*. 2000, **60**, 463.

(7) C. Rodriguez-Navarro, E. Ruiz-Agudo, A. Luque, A. B. Rodriguez-Navarro and M. Ortega-Huertas, *Am. Miner.* 2009, **94**, 578.

(8) T. H. Li and S. Gregory, *Geochim. Cosmochim. Acta* 1974, **38**, 703.

(9) D. K. Fisler and R. T. Cygan, *Am. Mineral*. 1999, **84**, 1392.

(10) J. R. Farver, R. A. Yund, *Contrib. Mineral. Petrol.* 1996, **123**, 77.